Supporting Information

Field-Induced slow magnetic relaxation and luminescence thermometry in a mononuclear ytterbium complex

Matilde Fondo,[a,] Julio Corredoira-Vázquez,[a] Ana M. García-Deibe,[a] Jesús Sanmartín-Matalobos,[a] Martín Amoza,[a] Alexandre M. P. Botas,[b] Rute A. S. Ferreira,[b] Luís D. Carlos[b,*] Enrique Colacio[c]*

[a] Departamento de Química Inorgánica, Facultade de Química, Universidade de Santiago de Compostela, Campus Vida, 15782 Santiago de Compostela, Spain.

[b] Phantom-g, CICECO – Aveiro Institute of Materials, Department of Physics, University of Aveiro, 3810-193 – Aveiro, Portugal

[c] Departamento de Química Inorgánica, Facultad de Ciencias, Universidad de Granada, Avda Fuentenueva s/n, 18071 Granada, Spain

Figure S1. TGA for **1**·2MeOH S3

Figure S2. Comparative powder X-ray diffractograms for **1**·2MeOH. Red: experimental diffractogram for the microcrystalline sample; green: calculated diffractogram using the data obtained from single X-ray diffraction studies**.** S3

Figure S3 Left) Frequency dependence of χ_M'' for **1**·2MeOH at 2.5 K in various applied fields. Right) Field dependence of the magnetic relaxation time at 2.5 K for **1**·2MeOH. S4

Figure S4. Frequency dependence of χ'_M for **1**·2MeOH (H_{ac} = 10 Oe) in H_{dc} = 1600 Oe at different temperatures. S4

Figure S5. Cole–Cole plot for **1**·2MeOH in H_{dc} = 1600 Oe. S4

Figure S6. Arrhenius plot for **1**·2MeOH in a dc applied field of 1600 Oe showing the Raman, Direct and combination of Raman-Direct fits. S5

Figure S7. Time-resolved emission spectra (acquired at 15 K excited at 360 nm) for starting delays of 0.01 (red line) and 0.02 ms (blue line). The emission spectrum measured in steady-state mode was scaled and is also shown for comparison. S5

Figure S8. Integrated intensity of areas I_1 (A) and I_2 (B). S6

Figure S9. Different views of the orientation of the main magnetic axis (Z) of the ground KD on Yb^{III} for **1**.2. S7

Figure S10. Estimation of the probability for different relaxation mechanisms of the spin between the two lowest energy KDs (black lines) in **1**.2: QTM and TA-QTM (green arrows); spin-phonon relaxation pathways (red and purple arrows). The values close to the arrows indicate the matrix elements of the transition magnetic moments. When this value is above 0.1 an efficient spin relaxation mechanism is expected. S7

Table S1. Main bond distances and angles for **1**·2MeOH. S8

Table S2. Crystal data and structure refinement for **1**·2MeOH.

Table S3. SHAPE v2.1. Continuous Shape Measures calculation (c) 2013 Electronic Structure Group, Universitat de Barcelona S9

Table S4. Some magnetic and structural information for field-induced Yb SIMs. S10-S11

Table S5. Energy (E, ± 5 cm^{-1}) and full-width-at-half maximum ($fwhm$, ± 5 cm^{-1}) of the $^2F_{5/2} \rightarrow {}^2F_{7/2}$ Stark components (identified from 1-4 and 1'-4') determined from the experimental emission spectrum (acquired at 11 K and excited at 360 nm) best fit (r^2>0.99) using a 8-components Gaussian function for **1**·2MeOH. S12

Table S6. Comparison of the energy differences obtain by electronic structure calculations (RASSCF/RASSI) and the luminescence studies (all in cm^{-1}). S12

Table S7. M_J Composition of the KD for **1**.1 and **1**.2 (all in %). S12

Table S8. Generalised Debye model fitting parameters for **1**·2MeOH S13

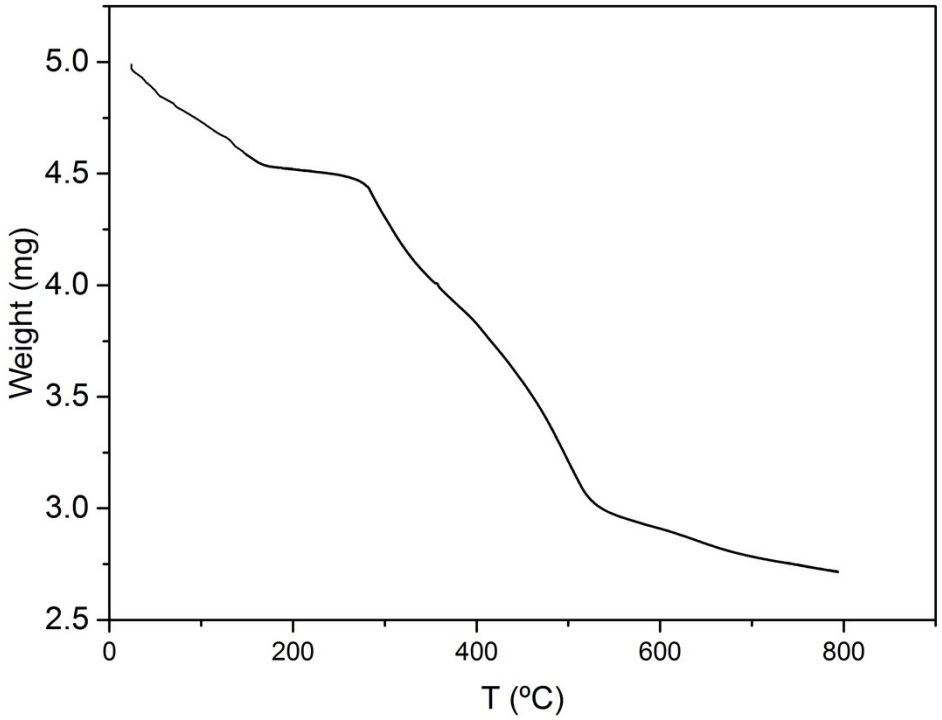

Figure S1. TGA for **1**·2MeOH.

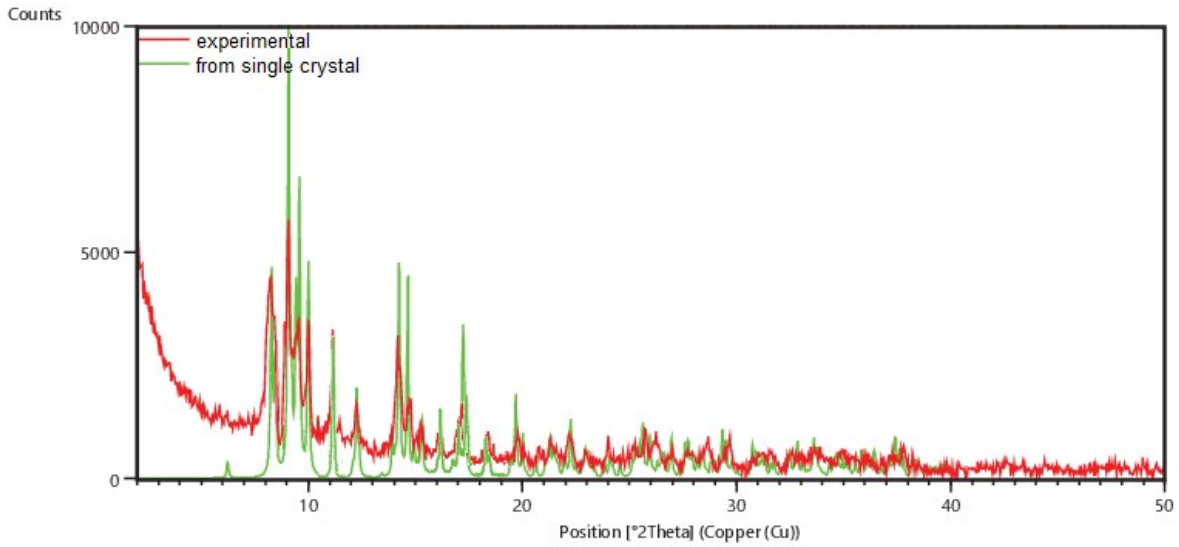

Figure S2. Comparative powder X-ray diffractograms for **1**·2MeOH. Red: experimental diffractogram for the microcrystalline sample; green: calculated diffractogram using the data obtained from single X-ray diffraction studies**.**

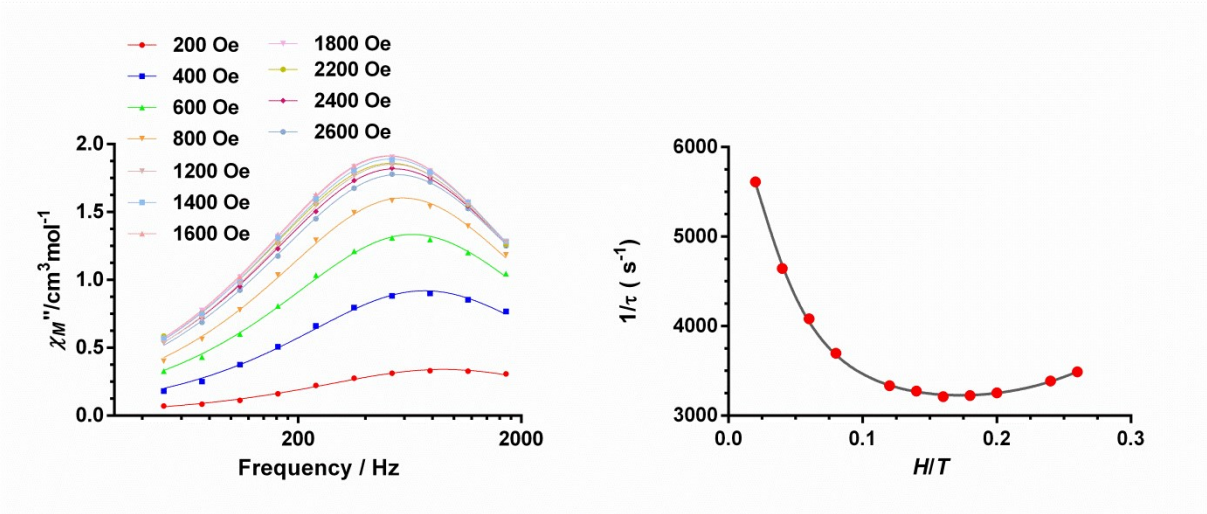

Figure S3 Left) Frequency dependence of χ_M'' for **1**·2MeOH at 2.5 K in various applied fields. Right) Field dependence of the magnetic relaxation time at 2.5 K for **1**·2MeOH.

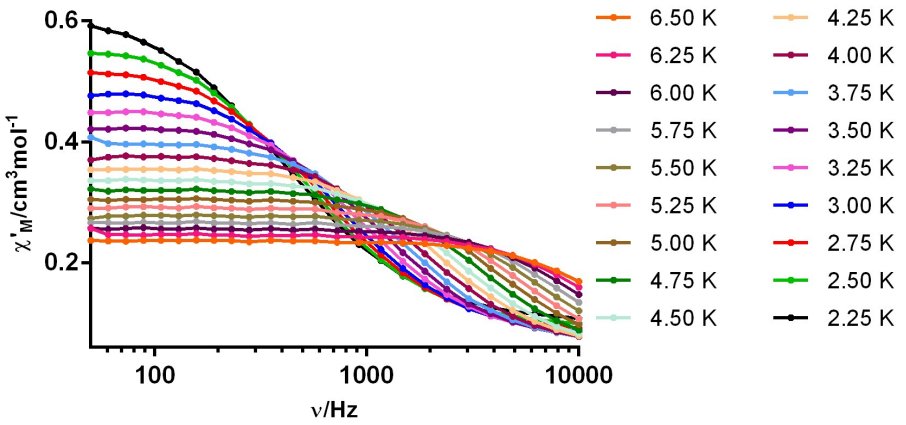

Figure S4. Frequency dependence of χ'_M for **1**·2MeOH (H_{ac} = 10 Oe) in H_{dc} = 1600 Oe at different temperatures.

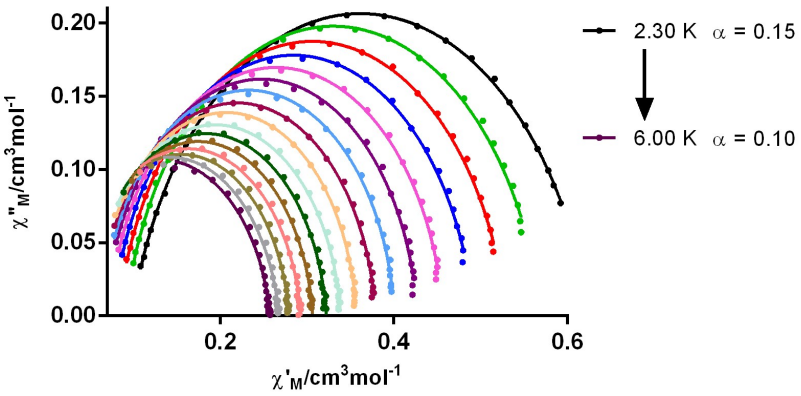

Figure S5. Cole–Cole plot for **1**·2MeOH in H_{dc} = 1600 Oe.

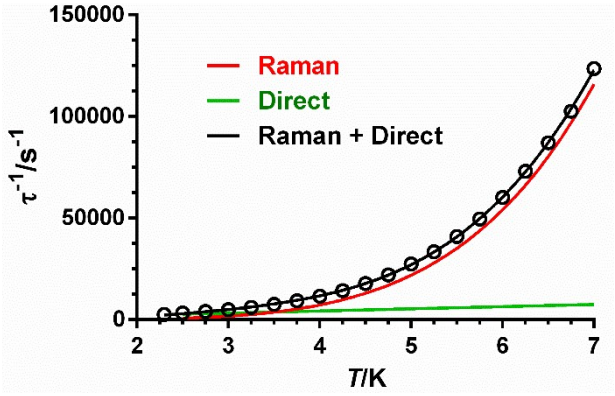

Figure S6. Arrhenius plot for **1**·2MeOH in a dc applied field of 1600 Oe showing the Raman, Direct and combination of Raman-Direct fits.

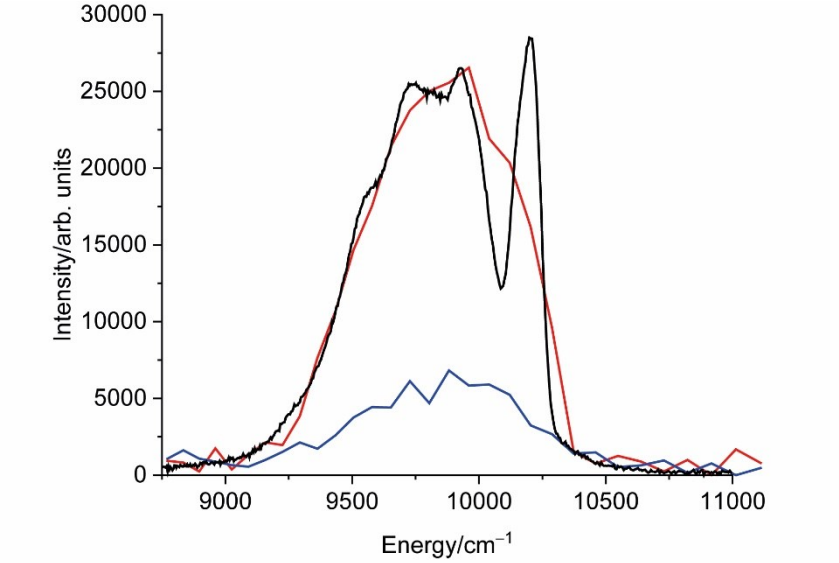

Figure S7. Time-resolved emission spectra (acquired at 15 K excited at 360 nm) for starting delays of 0.01 (red line) and 0.02 ms (blue line). The emission spectrum measured in steady-state mode was scaled and is also shown for comparison.

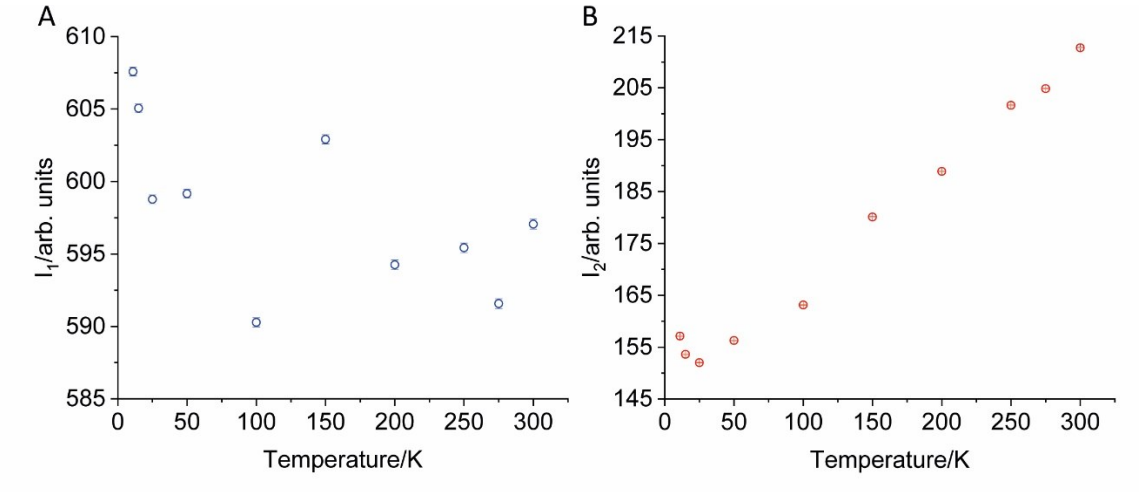

Figure S8. Integrated intensity of areas I_1 (A) and I_2 (B).

Temperature uncertainty ($\delta\Delta$) associated to the thermal readouts was obtained considering the experimental uncertainty associated with the thermometric parameter as:

$$(\delta\Delta)^2 = \left(\frac{\partial\Delta}{\partial I_1}\delta I_1\right)^2 + \left(\frac{\partial\Delta}{\partial I_2}\delta I_2\right)^2 = \left(\frac{-I_1}{{I_2}^2}\delta I_2\right)^2 + \left(\frac{1}{I_2}\delta I_1\right)^2 \qquad (S1)$$

where δ^{I_1} and $^{\delta I_2}$ are the uncertainties associated to of ^{I_1} and ^{I_2}, respectively. δ^{I_1} and $^{\delta I_2}$ were determined considering the standard error ($SE =$ 5×10⁻⁴) of the mean value of the noise signal of the spectrum (in the 10520-11111 cm^{-1} spectral range):

$$SE = \frac{\sigma}{\sqrt{N}} \qquad (S2)$$

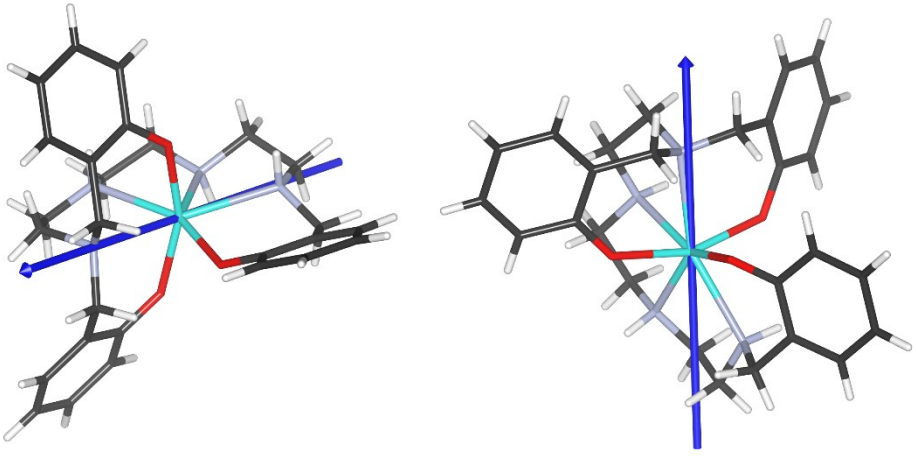

Figure S9. Different views of the orientation of the main magnetic axis (Z) of the ground KD on Yb^{III} for **1**.2.

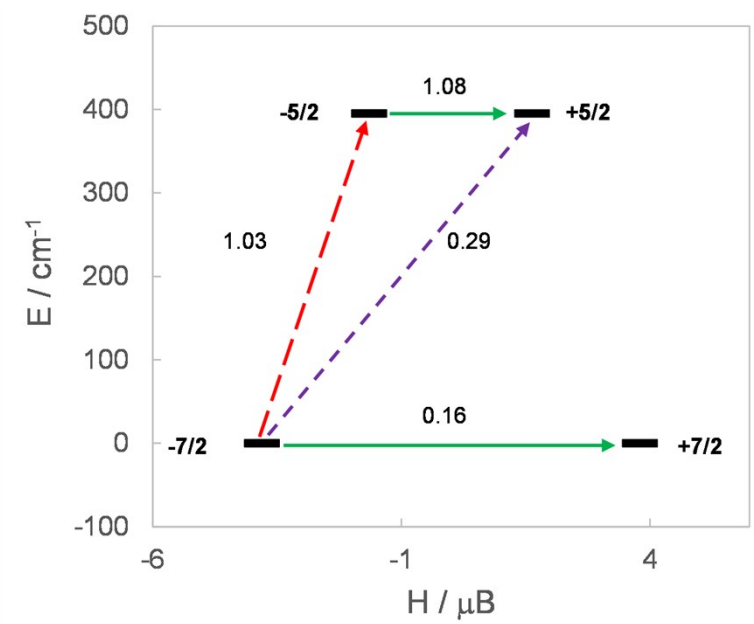

Figure S10. Estimation of the probability for different relaxation mechanisms of the spin between the two lowest energy KDs (black lines) in **1**.2: QTM and TA-QTM (green arrows); spin-phonon relaxation pathways (red and purple arrows). The values close to the arrows indicate the matrix elements of the transition magnetic moments. When this value is above 0.1 an efficient spin relaxation mechanism is expected.

Table S1. Main bond distances and angles for **1**·2MeOH.

1.1		**1.**2	
Yb1-O11	2.160(4)	Yb2-O21	2.158(4)
Yb1-O12	2.154(4)	Yb2-O22	2.156(4)
Yb1-O13	2.171(4)	Yb2-O23	2.169(4)
Yb1-N11	2.511(5)	Yb2-N21	2.532(5)
Yb1-N12	2.532(6)	Yb2-N22	2.520(5)
Yb1-N13	2.488(5)	Yb2-N23	2.501(5)
Yb1-N14	2.527(6)	Yb2-N24	2.539(5)
O12-Yb1-O11	160.46(17)	O22-Yb2-O21	159.83(16)
O13-Yb1-N11	83.40(16)	O23-Yb2-N21	83.43(15)
O13-Yb1-N14	75.03(17)	O23-Yb2-N24	75.56(16)
N11-Yb1-N12	67.68(18)	N22-Yb2-N21	67.99(16)
N13-Yb1-N12	68.18(19)	N23-Yb2-N22	68.19(16)
N13-Yb1-N14	68.6(2)	N23-Yb2-N24	68.63(18)

Table S2. Crystal data and structure refinement for **1**·2MeOH.

Empirical formula	$C_{29}H_{41}N_4O_5Yb$
Molecular weight	698.70
Crystal system	Orthorhombic
Space group	Pca_{21}
Wavelength (Å)	0.71073
Crystal size (mm^3)	0.130 x 0.080 x 0.060
Color, shape	Plate, yellow
T (K)	100(2)
a (Å)	20.7775(19)
b (Å)	14.5382(13)
c (Å)	19.7229(16)
α (º)	90
β (º)	90
γ (º)	90
Volume ($Å^3$)	5957.6(9)
Z	8
Flack parameter	-0.016(3)
Absorpt. coef. (mm^{-1})	3.182
Reflections collected	187658
Independent reflections	14817 [R(int) = 0.0672]
Data / restraints / param.	14817 / 1 / 714
Flack parameter	-0.016(3)
Final R indices [$I>2\sigma(I)$]	R_1 = 0.0279 wR_2 = 0.0611
R indices (all data)	R_1 = 0.0354 wR_2 = 0.0649

Table S3. SHAPE v2.1. Continuous Shape Measures calculation (c) 2013 Electronic Structure Group, Universitat de Barcelona

Geometries Coordination number 7

ETPY-7	7 C3v	Johnson elongated triangular pyramid J7
JPBPY-7	6 D5h	Johnson pentagonal bipyramid J13
CTPR-7	5 C2v	Capped trigonal prism
COC-7	4 C3v	Capped octahedron
PBPY-7	3 D5h	Pentagonal bipyramid
HPY-7	2 C6v	Hexagonal pyramid
HP-7	1 D7h	Heptagon

1·2MeOH

1.1

Structure [ML7]	JETPY-7	JPBPY-7	**CTPR-7**	COC-7	**PBPY-7**	HPY-7	HP-7
	18.667,	3.394,	**2.974**,	4.554,	**2.000**,	21.373,	31.806

1.2

Structure [ML7]	JETPY-7	JPBPY-7	**CTPR-7**	COC-7	**PBPY-7**	HPY-7	HP-7
	17.683,	3.715,	**2.726**,	4.161,	**2.371**,	21.202,	31.646

Table S4. Some magnetic and structural information for field-induced Yb SIMs.

Yb-SMM[a]	U_{eff}/K[c]	τ_0/s	*H*/Oe	*C. N. / Geometry*[d]	Best fit	Ref.[e]
$[Yb(H_3L^1)_2]Cl_3$[b]	5.76	2.0 X 10^{-5}	400	6 / OC	Raman-Direct	26
$Na[Yb(L^2)(H_2O)]$[a]	29	4.0 X 10^{-7}	1000	8 / SAPR	Orbach + Raman + Direct	27
$[Yb(murex)_3]$[a]	15.6	2.7 X 10^{-6}	2000	9 / CSAPR	nd	15
$[Yb(tta)_3(L^3)]$[a]	6	1.9 X 10^{-5}	1000	8 / SAPR	Orbach	16
$[Yb(L^4)_2](NO_3)$ [a]	5.37	1.0 X 10^{-5}	1000	8 / nd	Orbach	28
$[Yb(L^4)(tta)_2]$ [a]	16.1	1.8 X 10^{-7}	1000	8 / TDD	Orbach	28
[Yb(trensal)]	54.67	1.5 X 10^{-8}	2000	7 / CTPR	Raman-Direct	17
$[Yb(Tpz)_2(Bpz)]$ [a]	1-2	nd	1000	9 / JTCTPR	Orbach-Raman	29
[Cp*Yb(DAD)(THF)]	13.85	1.74 x 10^{-6}	1500	pseudo 4 / pseudo T	Orbach-Raman-Direct	30
$[Yb(L^5)_3]$[a]	11.7	4.6 x 10^{-6}	1000	9 / CSAPR	Raman	18
$[Yb(L^5)_2(tmh)(CH_3OH)]$[a]	29.7	3.5 x 10^{-7}	1000	9 / CSAPR	Raman	18
$[Yb(L^5)_2(tta)(CH_3OH)]$[a]	30.3	2.0 x 10^{-7}	1000	9 / CSAPR	Raman	18
$[Yb(PyrCOO)(acac)_2(H_2O)_2]$ [a]	55	2.1 × 10^{-8}	2000	8 / BTPR	Orbach-Direct	31
$[Yb(H_3Bmshp)(DMF)_2Cl_2]\cdot DMF\cdot 1.5H_2O$	14.5	2.38 × 10^{-5}	1500	7 / PBPY	Raman-Direct	32
$[Yb(H_3Bmshp)(DMF)_2Cl_2]\cdot H_4Bmshp$	43.8	3.83 × 10^{-7}	600	7 / PBPY	Orbach-Raman-Direct	32
$[Yb(NAS)_2(H_2O)_6](NAS)]$	45	5.1 × 10^{-8}	1000	8 / SAPR	Raman-QTM	33
$[Yb(depma)_2(H_2O)_6]Cl_3$	28.9	4.6 × 10^{-8}	750	8 / TDD	Orbach-Raman	19
$Yb(NO_3)_3(^tBu_3PO)_2$	23	6.8 × 10^{-7}	1000	8 / HPY	Raman-Direct	34
$[Yb(L^6)(OTf)_2](OTf)$	11.7	4.6 × 10^{-6}	1000	8 / TDD	Orbach-Raman	35

$[Yb(L^6)(NO_3)_3(MeOH)]$	17.8	8.7×10^{-7}	1000	9 / JCSAPR	Orbach-Raman	35
$[Yb(18\text{-crown-}6)(H_2O)_3](ClO_4)_3$	5.9	2.6×10^{-5}	500	9 / MMF	Orbach-Raman-QTM	36
$[Yb(H_2O)_5(NCS)_3]$	50	2.3×10^{-8}	2500	8 / BTPR	Raman	37
$[Yb(H_2O)(phen)_2(NCS)_3]$	22	4.5×10^{-7}	1000	8 / BTPR	Raman	37
$[Yb(H_2O)(bpy)_2(NCS)_3]$	47	1.7×10^{-8}	1000	8 / SAPR	Raman	37
$[Hbpy][Yb(bpy)_2(NCS)_4]$	44	2.9×10^{-8}	1000	8 / SAPR	Raman	37
$[Hbpy][Yb(phen)_2(NCS)_4]$	37	8.4×10^{-8}	1000	8 /SAPR	Orbach-Raman	37

[a] Solvate molecules omitted.

[b] H_3L^1= tris(((2-hydroxy-3-methoxybenzyl)amino)ethyl)-amine; $(L^2)^{4-}$ = anion of 1,4,7,10-tetraazacyclododecane-1,4,7,10-tetraacetic acid; $(murex)^-$ = murexide; L^3 = 4,5-ethylenedioxy-4',5'-bis(2-pyridyl-N-oxidemethylthio)tetrathiafulvalene; tta^- = 2-thenoyltrifluoroacetonate anion; $(L^4)^-$ = anion of rhodamine-6G-2-(hydrozinomethyl)quinolin-8-ol; H_3trensal = 2,2',2''-tris(salicylideneimino)triethylamine; Tpz = hydrotris(pyrazolyl)-borate; Bpz = dihydrobis(pyrazolyl)borate); DAD: $(2,6\text{-}Me_2C_6H_3NCHCHNC_6H_3Me_2\text{-}2,6]^{2-}$; Cp* = pentamethylcyclopentadiene; THF: tetrahydrofuran; $(L^5)^-$ anion of 2-(tetrazol-5-yl)-1,10-phenanthroline; tmh = 2,2,6,6-tetramethylheptanoate; $PyrCOO^-$ = pyrazine-2-carboxylate; H_4Bmshp = (2,6-bis[(3-methoxysalicylidene)hydrazinecarbonyl]-pyridine); NAS = 2-naphthalenesulfonate; depma = 9-diethylphosphonomethylanthracene; $^tBu_3PO$ = tritertbutylphosphine oxide; L^6 = 1-(1-methyl-2-((1-methyl-1H-imidazol-2-yl)methylene)hydrazineyl)-1-pyridine; OTf^- = triflate; 18-crown-6 = 1,4,7,10,13,16-hexaoxacyclooctadecane; bipy = 2,2'-bipyridine; phen = 1,10-phenantroline.

[c] U_{eff} values were taken from the best fit. If this fit does not include an Orbach process, then the U_{eff} values were calculated from a simple Arrhenius equation.

[d] CTPR: capped trigonal prism; SAPR: square antiprism¸ CSAPR: spherical capped square antiprism; JCSAPR: capped square antiprism; JTCTPR tricapped trigonal prism; MFF = muffin; BTPR: bicapped trigonal prism; TDD: triangular dodecahedron; HPY hexagonal bipyramidal; PBPY: pentagonal bipyramidal; OC = octahedron; T : tetrahedron.

[e] references in the paper.

nd = not described.

Table S5. Energy (E, ± 5 cm^{-1}) and full-width-at-half maximum ($fwhm$, ± 5 cm^{-1}) of the $^2F_{5/2} \rightarrow {}^2F_{7/2}$ Stark components (identified from 1-4 and 1'-4') determined from the experimental emission spectrum (acquired at 11 K and excited at 360 nm) best fit (r^2>0.99) using a 8-components Gaussian function for **1**·2MeOH.

Assignment*	***E***	***fwhm***
1	10220	52
1'	10166	54
2	9977	72
2'	9852	70
3	9720	74
3'	9560	69
4	9419	66
4'	9250	65

*The assignment is illustrated in Figure 7. The levels without ' correspond to unit **1**.1 and those with ' to unit **1**.2.

Table S6. Comparison of the energy differences obtain by electronic structure calculations (RASSCF/RASSI) and the luminescence studies (all in cm^{-1}).

Emision **1**.1*	Emision **1**.2**	RASSCF **1**.1	RASSCF 1.**2**
0	0	0	0
243	314	396	395
500	606	603	620
801	916	776	794

The energy values correspond to the difference between the E values (Table S5) between * 1 and 2, and ** 1' and 2'.

Table S7. M_J Composition of the KD for **1**.1 and **1**.2 (all in %).

	KD1		KD2		KD3		KD4	
	1.1	**1**.2	1.1	**1**.2	**1**.1	**1**.2	**1**.1	**1**.2
|±7/2>	**94.3**	**95**	2.8	2.2	1.3	1.5	1.6	1.3
|±5/2>	0.3	0.2	**68.5**	**69.8**	13.1	14	18	16
|±3/2>	2.7	2.3	20.2	20.4	**39.3**	**37.1**	**37.9**	**40.3**
|±1/2>	2.7	2.6	8.5	7.6	**46.3**	**47.5**	**42.5**	**42.3**

Table S8. Generalised Debye model fitting parameters for **1**·2MeOH

T/K	χ_S/(cm^{3}mol^{-1})	χ_T/(cm^{3}mol^{-1})	τ/(10^{-4}s)	α
2.30	0.098	0.63	3.86	0.15
2.50	0.090	0.57	3.07	0.12
2.75	0.083	0.53	2.50	0.11
3.00	0.076	0.49	2.02	0.10
3.25	0.072	0.46	1.64	0.08
3.50	0.068	0.43	1.32	0.07
3.75	0.065	0.40	1.07	0.06
4.00	0.060	0.38	0.86	0.06
4.25	0.058	0.36	0.70	0.05
4.50	0.050	0.34	0.56	0.06
4.75	0.046	0.32	0.45	0.07
5.00	0.043	0.31	0.36	0.07
5.25	0.034	0.29	0.30	0.08
5.50	0.031	0.28	0.24	0.08
5.75	0.016	0.27	0.20	0.10
6.00	0.007	0.26	0.17	0.10